Journal of
Materials Chemistry A
Materials for energy and sustainability

This article can be cited before page numbers have been issued, to do this please use: X. Zhang and E. Pomerantseva, *J. Mater. Chem. A*, 2025, DOI: 10.1039/D5TA00673B.

ROYAL SOCIETY
OF CHEMISTRY

rsc.li/materials-a

View Article Online
DOI: 10.1039/D5TA00673B

# Enhanced Cycling Performance of Bilayered Vanadium Oxide Cathode in Li-Ion Batteries via Dual Metal Ion Preintercalation

Xinle Zhang †, Ekaterina Pomerantseva †*

† *Department of Materials Science and Engineering, Drexel University, Philadelphia, PA 19104, USA*

* *Corresponding Author:* ep423@drexel.edu

**Keywords:** layered oxides; chemical preintercalation; annealing; cathodes; lithium-ion batteries.

## Abstract

Chemical preintercalation of $Li^+$ or $Mg^{2+}$ ions has showcased the capability to improve either specific capacity or cycling stability, respectively, of the bilayered vanadium oxide (BVO) electrode in Li-ion cells. However, advancing both properties in a single material via chemical preintercalation of both $Li^+$ and $Mg^{2+}$ ions has never been reported. Herein, we experimentally demonstrate that by simultaneously preintercalating electrochemically active $Li^+$ ions and structure stabilizing $Mg^{2+}$ ions, the specific capacity and cycling stability of BVO electrodes in lithium-ion cells can be synergistically improved. Additionally, we revealed the role of interlayer structural water in the charge storage and degradation mechanisms of dual metal ions preintercalated BVO electrodes. With the simultaneous preintercalation of 0.19 $Li^+$ ions and 0.10 $Mg^{2+}$ ions into the interlayer structure of BVO, the LMVO electrode demonstrated the specific capacity of ~245 mAh $g^{-1}$ in a potential window of 2.0-4.0 V (vs. $Li/Li^+$) with a capacity retention of 58% after 50 cycles. Low-temperature vacuum-drying at 200 °C reduced the hydration degree ($n$ in $\delta$-$Li_{0.19}Mg_{0.10}V_2O_5 \cdot nH_2O$) of LMVO, denoted as LMVO-200, from 0.85 to 0.67 per $V_2O_5$ without phase transformation, altered the charge storage mechanism from surface-controlled to diffusion-limited, and demonstrated further enhanced capacity retention of ~66% after 100 cycles. Additionally, via GITT experiments, we demonstrate that the dual metal ion preintercalation and vacuum-drying treatment lead to facilitated diffusion of $Li^+$ ions. Ex-situ XRD and ATR FTIR analyses of the LMVO-200 electrodes reveal their reversible bulk and local structure evolution during electrochemical operation, enabling excellent cycling stability in Li-ion cells. This work demonstrates a general strategy to synergistically enhance the specific capacity and cycling stability of layered oxide electrode materials for intercalation batteries.

View Article Online
DOI: 10.1039/D5TA00673B

# 1. Introduction

Rechargeable batteries are indispensable in modern society, powering our portable electronics and motivating the electrification of transport. They are experiencing a surge of demand for higher energy and power density that requires optimizing the structure and chemistry of the cathode materials to achieve higher capacity and longer lifespan [1-3]. Commercialized cathode materials in lithium-ion batteries, such as $LiFePO_4$ and $LiMn_2O_4$ spinel [4, 5] or layered $LiNi_xCo_yMn_zO_2$ and $LiNi_xCo_yAl_zO_2$ [6], usually deliver specific capacities below 200 mAh $g^{-1}$, and their capacity and cycling stability compromise in beyond lithium-ion battery systems [7, 8]. Moreover, the consumption of critical elements such as nickel (Ni) and cobalt (Co) in commercial cathode materials of lithium-ion batteries raises concerns regarding material sustainability [9]. Cathode materials based on layered vanadium oxides have demonstrated high capacity and versatility in a wide range of electrolyte systems [10-15] due to their spacious and tunable interlayer regions that enable fast intercalation and diffusion of various charge transport ions. In lithium-ion battery system, bilayered vanadium oxides (BVOs) can accommodate up to two $Li^+$ ions per unit cell when vanadium is reduced from $V^{5+}$ to $V^{4+}$ [10], enabling a high theoretical capacity of 294 mAh $g^{-1}$. However, maintaining such high capacity over extended cycling requires the preintercalation of inorganic metal ions [16-20] or organic species [21-23] to stabilize its large interlayer regions, so that the phase transformation [24], structural degradation [11], and electrochemical side reactions [25] during the electrochemical operation of BVO electrodes can be suppressed.

Chemical preintercalation is a versatile synthesis approach that enables inserting water-soluble foreign species into the interlayer regions of layered electrodes prior to electrochemical cycling, thereby enhancing the cathodic performance in multiple battery systems [26]. It has been shown that the single alkali or alkali-earth metal ions preintercalated BVOs ($\delta$-$M_xV_2O_5{\cdot}nH_2O$, where M stands for Li, Na, K, Mg, or Ca) enable improved cycling performance in lithium-ion [19, 20], sodium-ion [17, 27], potassium-ion [18], magnesium-ion [28], and calcium-ion [29] batteries with non-aqueous electrolytes. To understand the mechanisms of the chemical preintercalation effect, it has been proposed that the preintercalated metal ions can be distinguished as either electrochemically active (same as the electrolyte ions) or electrochemically inactive (different from the electrolyte ions) [26]. Chemical preintercalation of electrochemically active ions facilitates solid-state ion diffusion, thus leading to increased specific capacity; while chemical preintercalation of electrochemically inactive ions stabilizes the structure of electrode materials, thus improving the cycling stability [26]. For instance, in the non-aqueous lithium-ion cells, $\delta$-$Li_{0.51}V_2O_5{\cdot}nH_2O$ exhibited the highest initial specific capacity compared to other metal ions preintercalated phases, but it exhibited poor cycling stability due to the lack of structural stabilizing ions in the interlayer regions; while the $\delta$-$Mg_{0.37}V_2O_5{\cdot}nH_2O$ phase demonstrated the superior cycling stability in lithium-ion cells due to the stabilization effect of

View Article Online
DOI: 10.1039/D5TA00673B

electrochemically inactive $Mg^{2+}$ ions, however, the specific capacity was compromised [19, 20]. Therefore, the synthesis approach needs to be innovated to achieve synergistically enhanced capacity and stability for layered electrode materials by simultaneously preintercalating both electrochemically active and stabilizing ions.

It has been demonstrated that integrating two types of metal ions in layered vanadium oxides enhances their electrochemical cycling performance, but the mechanism and the role of chemically preintercalated ions remain elusive. One perspective ascribes that chemical preintercalated metal ions act as "pillars" that induce interlayer distance expansion [19, 30], thus altering the transport of the electrolyte ions from diffusion-controlled Faradaic process to surface-redox-controlled pseudocapacitive process [31]. Jiang et al. reported a Mn and Li "dual-ion-in-sequence" preintercalated vanadium oxide that led the interlayer distance to expand from 9.4 Å to 11 Å, which enhanced ion diffusivity and pseudocapacitive behavior that is favorable for aqueous zinc-ion energy storage [32]. Another study demonstrated that a large interlayer distance of 14.1 Å, achieved through the simultaneously preintercalating $K^+$ and $Mg^{2+}$ ions into the interlayer regions, synergistically enhanced the specific capacity and cycling stability of vanadium oxide electrode in zinc-ion cells [33]. Since then, widening the interlayer regions of layered vanadium oxides via preintercalating more than one type of monovalent, bivalent, or even trivalent metal ions has been demonstrated for enhancing the charge storage properties of layered vanadium oxides [14, 34-38]. In comparison, dual metal ion preintercalation also alters the confined chemical environment of the ion transport channels (interlayer regions of layered vanadium oxide), and therefore it might bring energy storage favorable features to electrode materials, such as improved redox reactivity or electronic conductivity. For instance, compared to the single $Ni^{2+}$ or $K^+$ preintercalated layered vanadium oxide electrodes, $Ni^{2+}$ and $K^+$ co-preintercalated electrode not only exhibited a higher capacitive charge contribution but also facilitated the electron transport and minimized the charge storage overpotential, leading to reduced charge transfer resistance, increased diffusion coefficient, and good electrochemical reversibility [39]. In addition, it has been shown that the confined $Na^+$ ions in the interlayer region of MXene-derived $\delta\text{-}Na_xK_yV_2O_5\cdot nH_2O$ electrode facilitated the desolvation of the neighboring electrochemically active $K^+$ ions and facilitated their diffusion in the electrode of non-aqueous potassium batteries [40]. Despite the preintercalation of $Li^+$ or $Mg^{2+}$ ions has demonstrated the capability of enhancing specific capacity or cycling stability separately, and a high capacity and cycling stability have been reported by using $V_2CT_x$ MXene as a precursor for chemical preintercalation synthesis with $Li^+$ or $Mg^{2+}$ ions [20], chemical preintercalation of layered vanadium oxide electrodes with both $Li^+$ and $Mg^{2+}$ ions to achieve high capacity and stability has never been experimentally demonstrated.

View Article Online
DOI: 10.1039/D5TA00673B

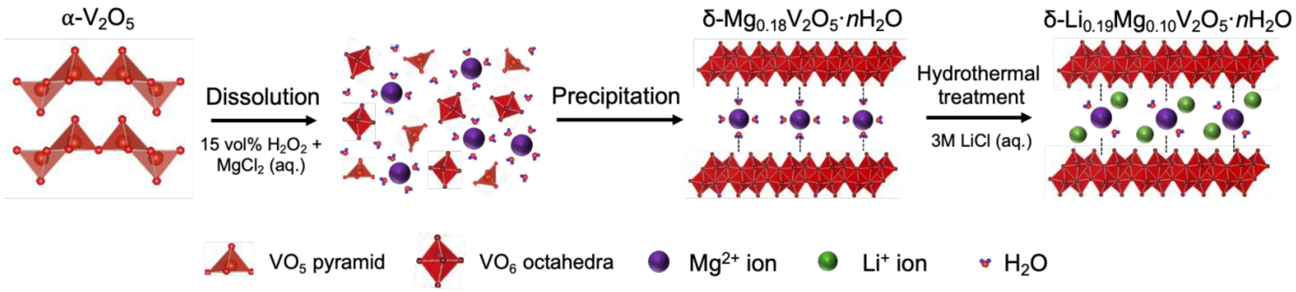

**Figure 1.** Synthesis schematics of dual $Li^+$ and $Mg^{2+}$ ions chemical preintercalation of bilayered vanadium oxide.

In this work, we developed an innovative synthesis approach to simultaneously chemically preintercalate electrochemically active $Li^+$ ions and stabilizing $Mg^{2+}$ ions within the structure of BVO. The amounts of chemically preintercalated $Li^+$, $Mg^{2+}$, and structural water per $V_2O_5$ were determined using atomic absorption spectroscopy (AAS) and thermogravimetric analysis (TGA), respectively, suggesting a chemical formula of $\delta$-$Li_{0.19}Mg_{0.10}V_2O_5\cdot 0.85H_2O$, denoted as LMVO. Additionally, low-temperature vacuum annealing was applied to LMVO, resulting in a reduced hydration degree ($\delta$-$Li_{0.19}Mg_{0.10}V_2O_5\cdot 0.67H_2O$, denoted as LMVO-200) without significantly altering its layered structure. The physical properties and electrochemical mechanisms of the LMVO and LMVO-200 polymorphs were studied in comparison to the $\delta$-$Li_{0.33}V_2O_5\cdot 0.88H_2O$ (LVO) and $\delta$-$Mg_{0.22}V_2O_5\cdot 0.92H_2O$ (MVO), demonstrating that the unique structure, morphology, chemistry, and enhanced electrochemical cycling performance can be achieved by tuning the chemically preintercalated metal ions and hydration degrees. Additionally, we conducted the ex-situ XRD and FTIR analyses of the post-cycled electrodes to further understand the material structural evolution and degradation during battery operation. By experimentally demonstrating the synergistically enhanced capacity and cycling stability of LMVO and LMVO-200 in lithium-ion cells achieved via dual-metal ions preintercalation strategy, we propose this methodology could be extended to other hydrated layered electrode materials and beyond lithium-ion battery systems.

View Article Online
DOI: 10.1039/D5TA00673B

# 2. Experimental Methods

## Dual Metal-Ion Chemical Preintercalation Synthesis

The LMVO was synthesized using a two-step approach including a wet chemical sol-gel step [41] followed by hydrothermal treatment illustrated in **Figure 1**. For the sol-gel step, 1.43 g of anhydrous $MgCl_2$ (99.9%, Thermo Scientific Chemicals) was dissolved in 15 mL of deionized water (ACS Reagent, Thermo Scientific) in a 250 mL beaker, followed by the addition of 15 mL of $H_2O_2$ (30 wt.% aq., Thermo Scientific) to form a transparent solution. 0.5 g of $V_2O_5$ powder (99.6%, Thermo Scientific) was slowly added into the solution over a span of 15 minutes, followed by stirring for an hour at room temperature to form a clear orange sol. Then, the temperature of the stirring plate was raised to 60 °C and kept at this value for another 4 hours to induce precipitation. After that, the beaker was covered with Parafilm in a fume hood to age the precipitate for 4 days as our previous work showed that the aging step is necessary to obtain a single bilayered phase [17]. The aged precipitate was thoroughly washed with deionized water through vacuum filtration, then transferred into a 23 mL Teflon-lined autoclave (Parr Instruments) and mixed with 15 mL of 3M LiCl (aq.) for hydrothermal treatment at 220 °C for 24 hours. The hydrothermally treated precipitate was thoroughly washed and filtered with deionized water, air-dried in a 105 °C oven for 24 hours, and denoted as LMVO. A portion of LMVO powder was treated in a vacuum oven at 200 °C for 24 hours and denoted as LMVO-200. For reference, the LVO phase was synthesized using a similar approach with 2.33 g of LiCl (98+%, Thermo Scientific Chemicals) added in the sol-gel step; the MVO phase was prepared via the same sol-gel step as LMVO powder, but it was hydrothermally treated in a 15 mL 0.5 M $MgCl_2$ (aq.) solution instead of LiCl solution used for the LMVO synthesis. Both reference materials were air-dried in a 105 °C oven for 24 hours.

## Physical Characterizations

X-ray diffraction (XRD) data were acquired using *Rigaku MiniFlex 600* with Cu-Kα radiation ($\lambda = 1.54$ Å) from $2\theta$ ranging from 3° to 40° with a step size of 0.02° and step duration of 0.5 s. Background of the diffraction patterns was subtracted using *CrystalDiffract 6* software. The amount of structural water in each sample was evaluated using Q50 thermogravimetric analyzer (TA instruments, USA) by measuring the weight loss from 100°C to 1000°C with a temperature ramp of 10°C $min^{-1}$, and the measurements were held at 100°C for 60 min to exclude the impact of physiosorbed water. FTIR pellets were prepared by hand-grinding 1 mg of the sample powder with 200 mg of KBr powder (ACS reagent, ≥ 99.0%) and press the powder in a 13 mm mold at 50 psi. FTIR spectra in transmission mode were recorded using an *INVENIO R* Spectrometer (Bruker, U.S.A.) between 400 and 4000 $cm^{-1}$. The stoichiometric formula of each sample was determined using a flame atomic absorption spectrometer (Shimadzu AA7000, Japan) equipped with

View Article Online
DOI: 10.1039/D5TA00673B

air-acetylene or nitroxide-acetylene burner for analyzing alkali-metal or transition-metal element, respectively. The AAS calibration curves were developed using standard solutions purchased from Inorganic Ventures, USA. The scanning electron microscopy (SEM) images were captured using *Apero 2S Low Vac* (ThermoFisher, USA) with 5 kV electron accelerating voltage captured using a trinity in-lens detector. XPS measurements were recorded on a Physical Electronics VersaProbe 5000 instrument using a monochromatic Al Kα source and ionized Ar for charge compensation. The high-resolution V *2p* spectra were taken at a pass energy of 23.5 eV with a step size of 0.05 eV. Peak fitting and data analysis were carried out using *CasaXPS* software. A Shirley background was used for V *2p* spectra quantification.

**Electrochemical Characterizations**

The electrode slurry was prepared by ground mixing 70 wt% of active material and 20 wt% carbon black (100% compressed, Thermo Scientific Chemicals), which was suspended in a NMP (99.5% 1-Methyl-2-pyrrolidinone, Acros Organics) solution with 10 wt% of *Kynar Flex* PVDF (Arkema, USA) in a polypropylene cup using *Flacktek SpeedMixer* (Flacktek, USA). The electrode slurry was cast onto the aluminum current collector using an 80 µm film applicator. The electrode films were dried at 105°C in the vacuum oven overnight, then punched to 10 mm electrode disks. The punched electrode disks were dried at 150°C in the vacuum oven for 24 h before being transferred into the glovebox to minimize the amount of structural water in the electrodes, following previously established procedure for hydrated oxides [42]. The electrodes were tested in type 2032 coin-cells with a two-electrode configuration, where 12 mm lithium metal disks served as both counter and reference electrodes, 16 mm polymer films served as separator (Celgard 2325, USA), and 1 M $LiPF_6$ in EC/DEC (Gotion Inc, USA) was used as electrolyte. The electrochemical properties were evaluated within a voltage window of 2.0-4.0 V, using multichannel potentiostat (Biologic VMP3, USA) and electrochemical workstation (Arbin Instruments, USA). All potentials in this work are reported with respect to the $Li/Li^+$ reference electrode. The cyclic voltammetry curves were acquired using scan rates of 0.1, 0.2, 0.4, 0.6, 0.8, and 1 mV $s^{-1}$, respectively. The cycle life test was conducted by galvanostatically cycling the cells with a current density of 20 mA $g^{-1}$, and the rate capabilities were assessed by cycling for 10 cycles at each of 20, 50, 100, 200, and 20 mA $g^{-1}$ current densities at room temperature, respectively. To analyze the charge storage contributions due to the surface-controlled and diffusion-limited processes, cyclic voltammetry curves were acquired at multiple scan rates from 0.1 mV $s^{-1}$ to 1mV $s^{-1}$. The measured peak current ($i$) and scan rate ($v$) complies the following relationship:

$$i = av^b$$

$$\text{thus, } \log(i) = \log(a) + b\cdot\log(v)$$

View Article Online
DOI: 10.1039/D5TA00673B

By determining the slope of log($i$) versus log($v$) in the experimental data fitted to the equation above, the b-value was calculated. The b-value typically ranges from 0.5 to 1.0 and indicates the proportion of the diffusion-limited charge storage process (b=0.5) and surface-controlled charge storage process (b=1.0).

The GITT experiments consisted of 1800 s (30 min) of discharge periods at a current density of 10 mA $g^{-1}$ and 72000 s (1200 min) of rest periods, which left the cells at open circuit to reach the equilibrium states. The diffusion coefficients of $Li^+$ ions ($D_{Li^+}$) were derived using the following equation [43, 44]:

$$D_{Li^+} = \frac{4}{\tau\pi}\left(\frac{n_m V_m}{S}\right)^2\left[\frac{\Delta E_e}{\Delta E_\tau}\right]^2 \left(\tau \ll \frac{L^2}{D_{Li^+}}\right)$$

Where $n_m$ and $V_m$ are the moles and molar volumes ($cm^3$ $mol^{-1}$) of the hybrid BVOs, respectively; $S$ is the geometric area of the electrodes ($cm^2$); $\Delta E_e$ and $\Delta E_\tau$ are the voltage differences between the equilibrium states and the voltage drop due to the application of a discharge current in a period of $\tau$ (1800 s).

### Ex-situ XRD and FTIR analysis

The Li-ion cells containing LMVO-200 electrodes were cycled using a multichannel potentiostat (Biologic VMP3, USA) at the cut-off potentials of 3.6 V (open circuit potential), 2.7 V, 2.0 V (during 1st discharge), 3.0 V, and 4.0 V (during 1st charge) via linear sweep voltammetry (LSV) at a scan rate of 0.05 mV $s^{-1}$. A relatively slow scan rate was chosen in order to minimize the hysteresis effect during the electrochemical operation. The electrochemically cycled cells were disassembled in an argon-filled glovebox, and the working electrodes were air-dried at 105°C after being rinsed three times with dimethyl carbonate (99+%, Thermo Scientific Chemicals) prior to the ex-situ XRD and FTIR analyses. The ex-situ XRD patterns were acquired using a *Rigaku MiniFlex 600* with Cu-Kα radiation ($\lambda$ = 1.54 Å) over a 2θ range from 3° to 40°, with a step size of 0.02° and a step duration of 1.0 s. The attenuated total reflectance (ATR) mode was employed to non-destructively obtain the FTIR spectra of the ex-situ electrodes, using an *INVENIO R* Spectrometer (Bruker, USA) scanned between 400 and 4000 $cm^{-1}$.

View Article Online
DOI: 10.1039/D5TA00673B

## 3. Results and Discussions

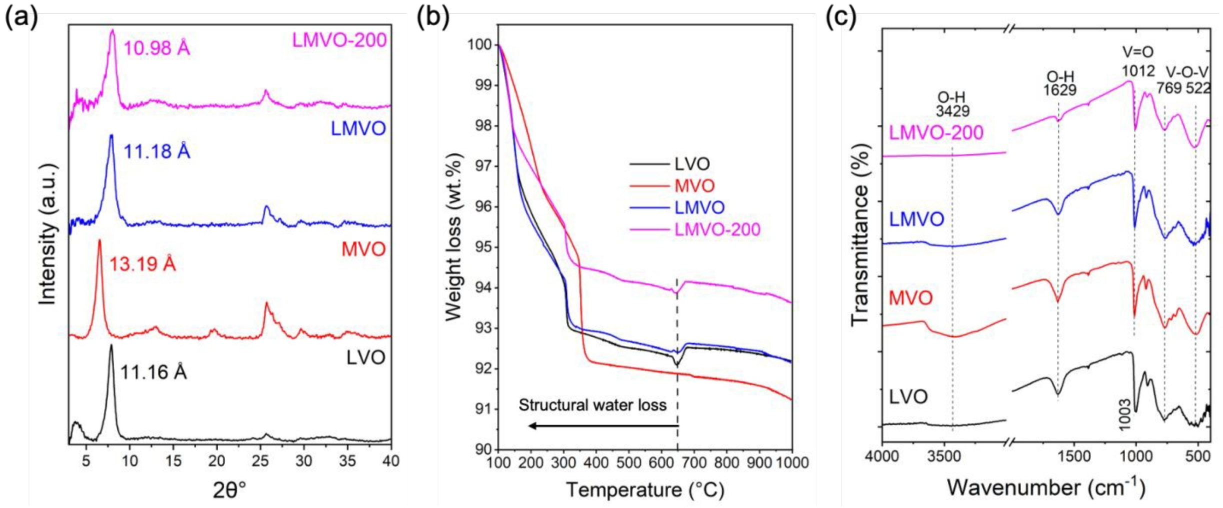

**Figure 2.** (a) XRD patterns, (b) TGA weight loss curves, and (c) FTIR spectra of LVO, MVO, LMVO, and LMVO-200 phases.

The XRD patterns of LVO, MVO, LMVO, and LMVO-200, shown in **Figure 2 (a)**, confirm that the chemical preintercalation synthesis performed in this work yields nanostructured bilayered vanadium oxides with varying interlayer distances that depend on the type of metal ions present in the sol-gel and hydrothermal treatment steps. The *d*-spacings of LVO and MVO, calculated from the positions of (001) peaks are 11.16 Å and 13.19 Å, respectively. These values are consistent with the previously reported δ-$Li_{0.51}V_2O_5{\cdot}nH_2O$ and δ-$Mg_{0.37}V_2O_5{\cdot}nH_2O$ phases and correspond to the BVO structures preintercalated with hydrated $Li^+$ or $Mg^{2+}$ ions, respectively [16, 19, 20]. The joint analysis of TGA (**Figure 2b**) and AAS (**Figure 3**) were conducted to determine the stoichiometry between lithium, magnesium, vanadium, and structural water in the chemically preintercalated polymorphs in this work, as listed on **Table 1**. The contents of structural water in each sample were determined by evaluating the weight loss characteristics from 100 to 650 °C. The stoichiometries of the LVO and MVO reference materials in this work were determined as δ-$Li_{0.33}V_2O_5{\cdot}0.88H_2O$ and δ-$Mg_{0.22}V_2O_5{\cdot}0.92H_2O$, respectively. The LMVO phase that was synthesized with both $Li^+$ and $Mg^{2+}$ ions shows an interlayer distance of 11.18 Å that is similar to that of the LVO phase, but the AAS and EDS (**Supporting Information, Figure S1**) analysis suggest that LMVO possesses both lithium and magnesium elements with a stoichiometry of $Li_{0.19}Mg_{0.10}V_2O_5{\cdot}0.85H_2O$. The MVO obtained from the sol-gel step (denoted as MVO-aged), which is the precursor of LMVO prior to hydrothermal treatment, was determined to have a formula of δ-$Mg_{0.18}V_2O_5$ (**Supporting Information, Figure S2**). Comparing the magnesium content in MVO-aged ($Mg_{0.18}$) and LMVO ($Mg_{0.10}$), it reveals that $Mg^{2+}$ ions in MVO-aged were partially exchanged with $Li^+$ ions from the LiCl solution during the hydrothermal treatment. The XRD analysis indicated that vacuum drying of LMVO at 200°C (LMVO-200) caused the *d*-

View Article Online
DOI: 10.1039/D5TA00673B

spacing to reduce from 11.18 Å to 10.98 Å without phase transformation, and the TGA analysis indicates that the ~0.2 Å decrease in *d*-spacing correspond to the dehydration of LMVO from *0.85* to *0.67* $H_2O$ per $Li_{0.19}Mg_{0.10}V_2O_5$. The XRD and TGA analyses confirmed that the interlayer distance is dominated by the hydration degree of the interlayer regions ($n$ in $\delta$-$M_xV_2O_5\cdot nH_2O$), which can be impacted by the nature of metal ions introduced during the chemical preintercalation synthesis. Moreover, the TGA curves of LVO, LMVO, and LMVO-200 samples exhibited weight regaining characteristics at temperatures between 650 to 680 °C, suggesting the presence of the oxygen vacancies in these samples that were refilled by air oxygens during the TGA measurement [20, 27, 45]. The FTIR spectra, shown in **Figure 2c**, were acquired to understand the characteristics of structural water and the V-O in-plane structures. The normalized intensity of water bands at ~1629 $cm^{-1}$ (O-H bending) and 3629 $cm^{-1}$ (O-H stretching) aligns with the hydration degrees determined via TGA weight loss analysis: MVO exhibits the highest intensity, LVO and LMVO show comparable but lower intensities, and the most dehydrated LMVO-200 phase displays the weakest structural water characteristics (**Figure 2c**). Additionally, the FTIR spectra exhibited the fingerprint region of bilayered vanadium oxide, including the V-O-V out-plane stretching, V-O-V in-plane stretching, and V=O stretching bands at 522, 769, and 1012 $cm^{-1}$, respectively, confirmed the bilayered intra-layer structure of all samples in this study [27, 45, 46].

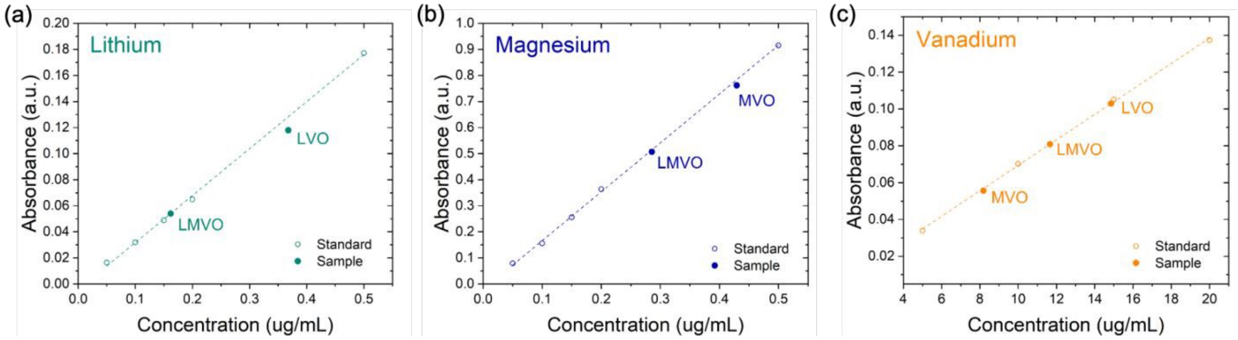

**Figure 3.** AAS calibration curves for (a) lithium, (b) magnesium, and (c) vanadium as well as the absorbances of the AAS samples prepared with LVO, MVO, and LMVO that correspond to the concentrations of each element.

**Table 1.** Li:V and Mg:V ratios (at.%) determined via AAS, weight loss of structural water (wt.%) determined via TGA, and stoichiometry of LVO, MVO, LMVO, and LMVO-200 according to AAS and TGA analyses.

| Sample name | Li:V ratio (via AAS) | Mg:V ratio (via AAS) | Structural water loss (wt.%, via TGA) | Chemical Formula |
|---|---|---|---|---|
| LVO | 0.1666 | N/A | 7.90 | $\delta$-$Li_{0.33}V_2O_5\cdot\mathit{0.88}H_2O$ |
| MVO | N/A | 0.1098 | 8.12 | $\delta$-$Mg_{0.22}V_2O_5\cdot\mathit{0.92}H_2O$ |
| LMVO | 0.0971 | 0.0511 | 7.60 | $\delta$-$Li_{0.19}Mg_{0.10}V_2O_5\cdot\mathit{0.85}H_2O$ |
| LMVO-200 | 0.0971 | 0.0511 | 6.12 | $\delta$-$Li_{0.19}Mg_{0.10}V_2O_5\cdot\mathit{0.67}H_2O$ |

View Article Online
DOI: 10.1039/D5TA00673B

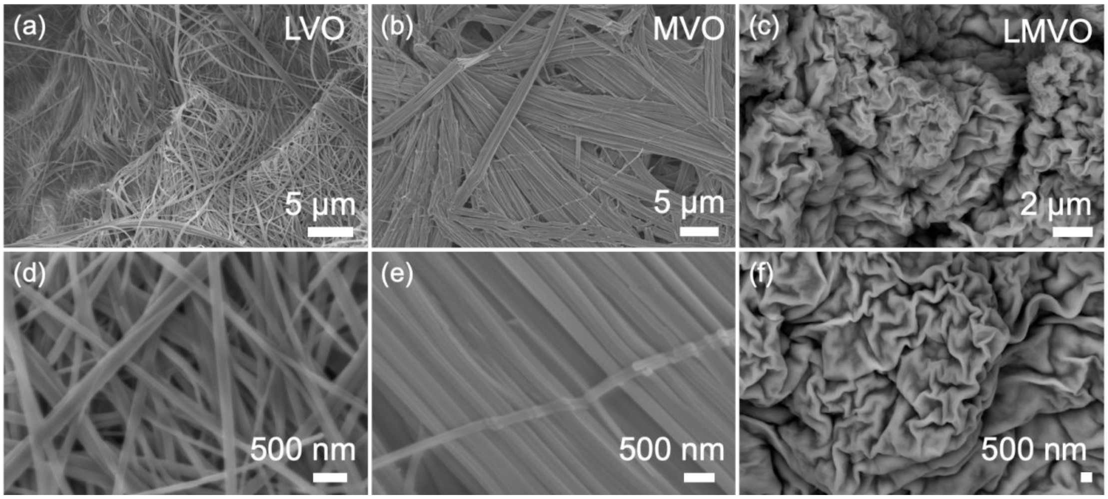

**Figure 4.** (a-c) Low magnification and (d-f) high magnification SEM images of (a, d) LVO, (b, e) MVO, (c, f) LMVO phases.

**Figure 4** shows SEM images of LVO, MVO, and LMVO particles at low and high magnifications. Consistent with literature, the SEM images indicate that LVO and MVO particles represent approximately 200 nm wide one-dimensional (1D) nanobelts [19]. However, the nanobelts in the SEM images of LVO appear more disordered and entangled, while those in the SEM images of MVO are straighter, better aligned, and packed parallel to each other. Simultaneous preintercalation of lithium and magnesium ions, leads to drastic changes of the morphology: LMVO powder is composed of crumpled nanosheets. It appears that chemical preintercalation of $Li^+$ and $Mg^{2+}$ ions simultaneously induces the transformation of 1D nanowires into two-dimensional (2D) crumpled nanosheets, and according to the literature, 2D morphology typically offers superior electrochemical cycling stability to BVO compared to 1D nanowires with similar chemistries [20, 47]. The SEM images imply that the transition of morphology from 1D to 2D could be a factor that contributes to the electrochemical cycling stability of LMVO.

View Article Online
DOI: 10.1039/D5TA00673B

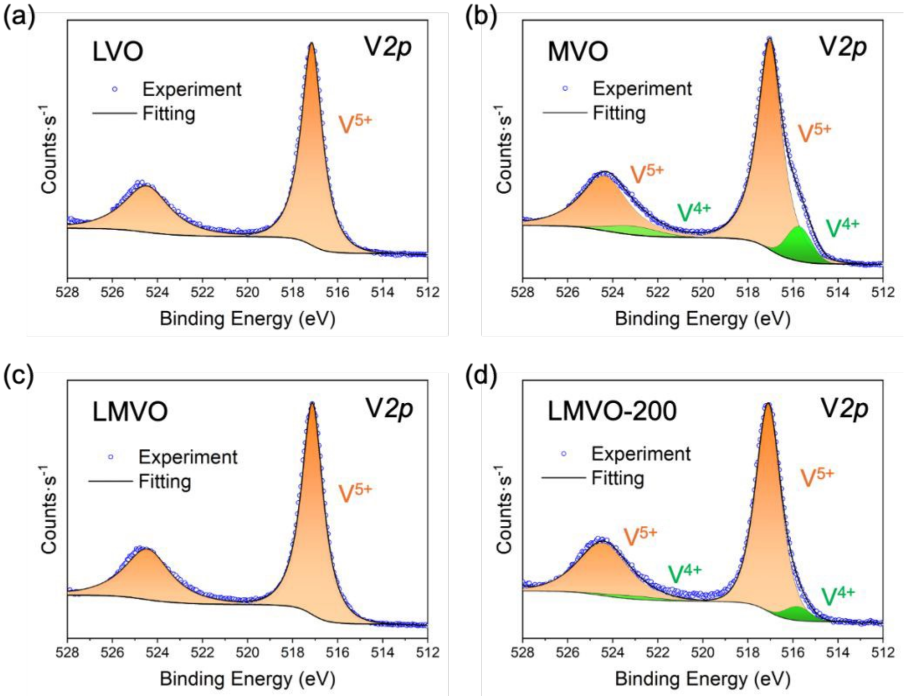

**Figure 5.** XPS spectra and fittings in V2p region of (a) LVO, (b) MVO, (c) LMVO, and (d) LMVO-200.

To study the influence of the chemical preintercalation of metal ions on the vanadium oxidation states, XPS spectra in the V2p region of LVO, MVO, LMVO, and LMVO-200 were analyzed and shown in **Figure 5**. The peaks at binding energies of ~517.2 and ~524.5 eV correspond to the V2p$_{3/2}$ and V2p$_{1/2}$ characteristics of V$^{5+}$, respectively. Due to the preintercalation of positively charged metal ions, the V2p$_{3/2}$ and V2p$_{1/2}$ characteristics from V$^{4+}$ were identified in the V2p region of MVO and LMVO-200 at binding energies of ~515.8 and ~523.2 eV. The XPS spectra suggest no vanadium reduction occurred to LVO and LMVO, revealing the strong charge-shielding effect of structural water [48-50], which is located at the interlayer regions and surrounded the chemically preintercalated Li$^+$ and Mg$^{2+}$ ions. We believe the structural water in MVO mitigated the vanadium reduction by the same charge-shielding effect, but the charges carried by the chemically preintercalated Mg$^{2+}$ ions were not fully neutralized, therefore led to the reduction of vanadium. After vacuum-drying at 200 °C, the formation of V$^{4+}$ in LMVO-200 implies the introduction of additional bonds and increased stacking order of the bilayers, which have been demonstrated to improve electrochemical stability during battery operation [27]. The XPS analysis revealed that the vanadium in LVO and LMVO can be electrochemically reduced from the highest valance state during battery operation, thus enabling their relatively high specific capacity compared to MVO and LMVO-200, respectively, which vanadium reduction has been incurred during synthesis. To further understand the characteristic of oxygen and oxygen vacancies, the XPS spectra in O1s region are shown in **Supporting Information, Figure S3**. According to the XPS O1s spectra, all samples show characteristic of V-O lattice oxygen at ~530 eV, and

View Article Online
DOI: 10.1039/D5TA00673B

two shoulder peaks at binding energies of ~531.2 and ~532.5 eV, which correspond to the characteristics of oxygen vacancies and structural water, respectively [14, 51]. The presence of oxygen vacancy characteristics in the O1s spectra of LVO, LMVO, and LMVO-200 agree with the presence of weight regaining characteristics observed at 650 to 680 °C in TGA curves. Additionally, other oxygen characteristics in O1s XPS spectra such as water-oxygen substituted oxygen vacancies also show significance in electrochemical applications. For example, the O1s XPS spectrum suggests the presence of the oxygen vacancies in MVO (**Supporting Information, Figure S3b**), but no refill of oxygen vacancies (weight regaining characteristic) observed in its TGA weight loss curve. This observation indicates the oxygen vacancies in the V-O sublattice of MVO might be occupied by structural water oxygens, similar to the characteristic reported in layered molybdenum oxides [52, 53], and leading to no weight regaining characteristic in its TGA weight loss curve.

View Article Online
DOI: 10.1039/D5TA00673B

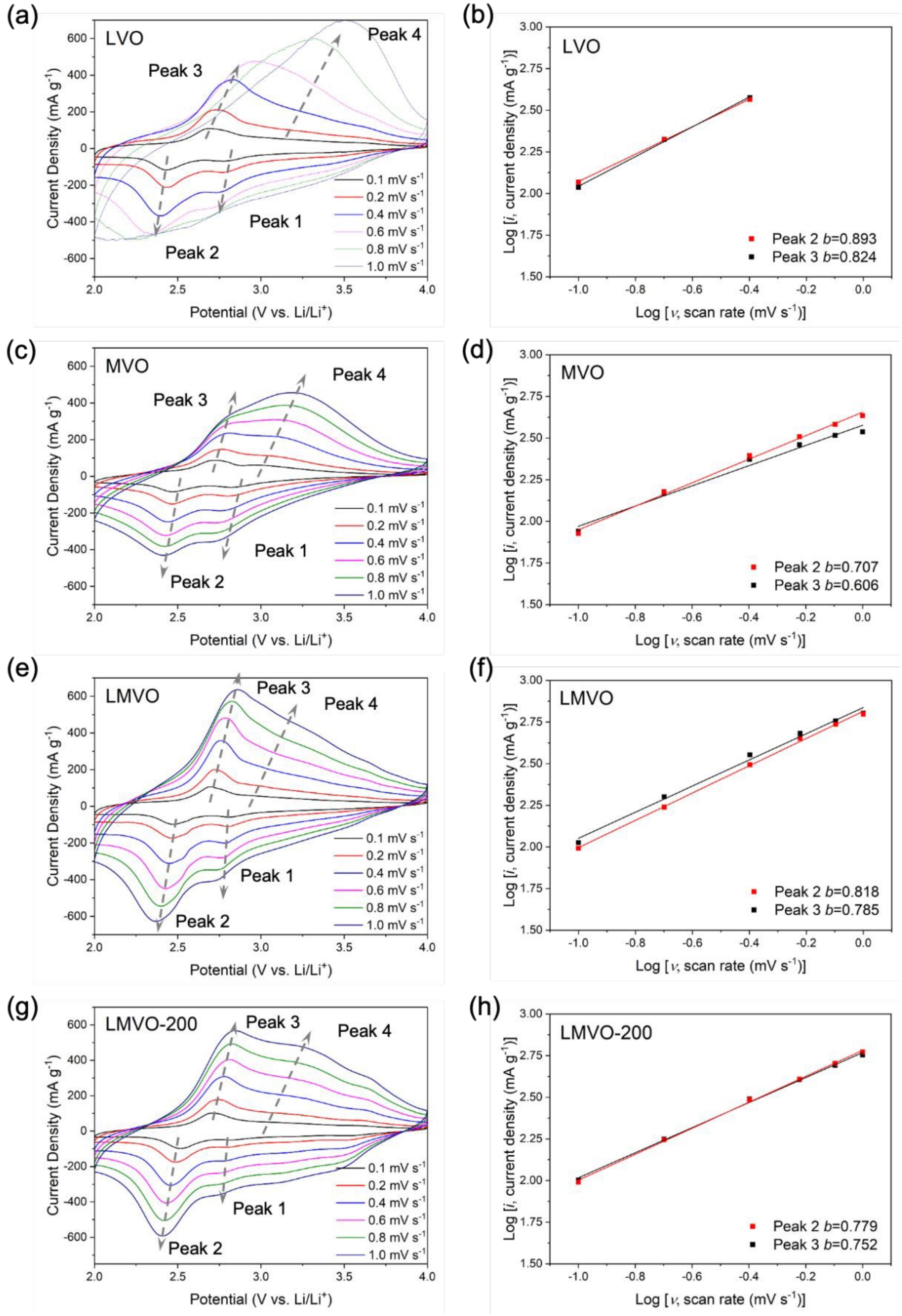

**Figure 6.** Sweep rate-dependent cyclic voltammetry study of (a, b) LVO, (c, d) MVO, (e, f) LMVO, and (g, h) LMVO-200 electrodes. (a, c, e, g) CV curves with scan rates of 0.1, 0.2, 0.4, 0.6, 0.8, and 1.0. mV s$^{-1}$, and (b, d, f, h) *b* values that were derived from the Log *i* vs. Log *v* profiles at the peak current densities of corresponding CV curves.

View Article Online
DOI: 10.1039/D5TA00673B

The CV curves at the scan rates of 0.1 – 1.0 mV·s$^{-1}$, demonstrated in **Figure 6**, suggest that four samples underwent similar two-step redox processes between 2.0 – 4.0 V. At a scan rate of 0.1 mV s$^{-1}$, the first cathodic/anodic pair is located at ~2.45/2.80 V (peak 2/peak 3), and another cathodic peak appears at ~2.80 V (peak 1) with a broad shoulder anodic peak at above 3.0 V (peak 4). As the scan rate increases, all cathodic/anodic peaks in CV curves shift to lower/higher potentials due to charge polarization effect. We performed the b-value analyses for peak 2 & 3 (peak 1 & 4 are too broad to reliably identify their potentials), shown in **Figure 6, (b, d, f, h),** to further understand the charge storage mechanism. Since the peaks in the CV curves of LVO broadened and shifted significantly when the scan rate increased to 0.6 mV s$^{-1}$, the fitting of the *b* value for LVO is only taken from the cycles with scan rates of 0.1, 0.2, and 0.4 mV s$^{-1}$. Peaks 2 and 3 of LVO, labeled in **Figure 6 (a)**, were determined the *b*-values of 0.893 and 0.824, respectively, indicating a pseudocapacitive characteristic dominated by surface-controlled capacitive processes. The two anodic peaks in MVO exhibit a strong rate-dependent behavior, as the peak 3 dominates the anodic process at low scan rates (0.1 – 0.4 mV s$^{-1}$), but it was surpassed by peak 4 at higher scan rates (0.6-1.0 mV s$^{-1}$). The b-value analysis reveals that the peak 2/3 in MVO is dominated by diffusion-limited process (b=0.707/0.606). As the scan rate increases (> 0.6 mV s$^{-1}$), the peak 1 & 4 in MVO broadening significantly, which suggest the surface-controlled process gradually dominates the charge storage mechanism. This observation suggests the peak 1 & 4 in MVO possibly involves the pseudocapacitive processes mediated by structural water at high scan rates [54, 55]. The peak 2 & 3 in CV curves of MVO, were suggested to have smaller *b* values compared to those of LVO, revealing that a more diffusion-limited kinetics could be enabled by preintercalating electrochemically inactive $Mg^{2+}$ ions. The *b* values of the three peaks in LMVO are between those of LVO and MVO, suggesting that the chemically preintercalated $Li^+$ ions are electrochemically active and effectively facilitate ion diffusion. Peaks 2 and 3 of LMVO were determined to have *b* values of 0.818 and 0.785, respectively. These values decreased to 0.779 and 0.752 after vacuum-drying at 200°C (as shown by LMVO-200, **Figure 6h**), indicating that the removal of structural water mitigated the charge-shielding effect of structural water in LMVO-200, therefore diminished the surface-controlled charge storage contribution [49, 50, 54, 55].

View Article Online
DOI: 10.1039/D5TA00673B

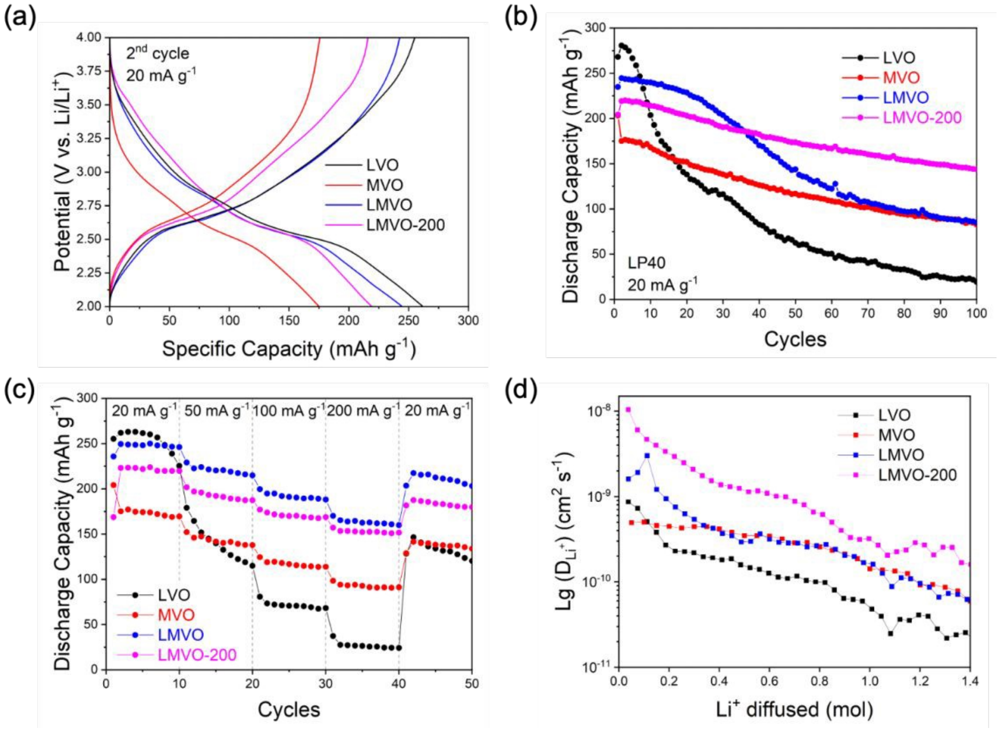

**Figure 7.** Galvanostatic cycling results for LVO, MVO, LMVO, and LMVO-200 electrodes: (a) charge-discharge profile of the 2nd cycles, (b) cycling stability for 100 cycles, (c) rate capabilities at current densities of 20, 50, 100, 200, and 20 mA $g^{-1}$ (electrodes were cycled at each current density for 10 cycles), and (d) $Li^+$ diffusion coefficients derived from the GITT experiments.

To further investigate the effects of dual metal-ion preintercalation on specific capacity and cycling stability, electrochemical cycling tests were conducted in Li-ion cells containing the LMVO and LMVO-200 electrodes, using LVO and MVO electrodes as references. **Figure 7 (a)** shows the 2nd cycle galvanostatic charge-discharge profiles of each electrode, indicating their specific capacities in the initial state. The discharge curves exhibit two plateaus at ~2.80 and ~2.45 V, the charge curves exhibit one plateau at ~2.80 V, in agreement with the potentials of the redox peaks observed in the CV curves (0.1 mV $s^{-1}$). The LMVO electrode exhibited an initial specific capacity of 244.55 mAh $g^{-1}$, which is between that of LVO and MVO, suggesting that the specific capacity and cycling stability of the BVO electrodes are tunable by controlling the chemistry of the interlayer region. After partially removing structural water from LMVO via vacuum annealing at 200°C, the LMVO-200 electrode showed initial discharge capacity of 223 mAh $g^{-1}$, which decreased by ~20 mAh $g^{-1}$ compared to LMVO electrode. This trend could be attributed to the decreased interlayer distance and surface-controlled capacitive contribution due to dehydrating the interlayer regions, implied by the XRD pattern and b-value analysis above. **Figure 7 (b)** shows the comparison of the cycling stabilities within 100 discharge cycles at a fixed current density of 20 mA $g^{-1}$. The LMVO electrode, containing 0.19 $Li^+$ and 0.10 $Mg^{2+}$ per $V_2O_5$, exhibited the stabilization effect of $Mg^{2+}$ without significantly

View Article Online
DOI: 10.1039/D5TA00673B

compromising specific capacity due to the concurrent preintercalation of $Li^+$ ions. The LMVO-200 electrodes, which were partially dehydrated compared to LMVO, demonstrated the highest electrochemical cycling stability in this work, retaining ~66% of the specific capacity relative to its initial state after 100th cycle. The enhanced electrochemical stability of LMVO-200 is attributed to its most dehydrated interlayer regions enabled by vacuum-drying, which suppresses the structural water involved parasitic reaction such as irreversibly produces electrochemically inactive LiOH during the electrochemical cycling [25].

Ex-situ XRD analysis of the electrodes after 20 galvanostatic cycles at 20 mA $g^{-1}$ (**Supporting Information, Figure S4**) were conducted to understand the degradation mechanism of the BVO polymorphs in this work. Before cycling, the interlayer distances of the active material in pristine electrodes (**Supporting Information, Figure S4a)** vary from ~11 to ~13 Å, which generally agrees with the interlayer distances calculated from the powder XRD patterns (**Figure 2a**). After 20 cycles, the XRD patterns of the post-cycling electrodes (**Supporting Information, Figure S4b)** suggest that their interlayer distances declined to ~10.8 Å regardless of the chemistry the interlayer regions, possibly implying that the extraction of varying amounts of structural water occurred during the electrochemical cycling. This finding underscores the importance of minimizing interlayer structural water without inducing phase transformation to mitigate the cathode-originated structural water shuttling effect. Additionally, the XRD patterns of the electrodes after 20 cycles maintained good shape and intensity of their (001) peaks, suggesting that all four polymorphs were able to retain their layered structure during the first 20 cycles. The ex-situ XRD analysis of the post-cycling electrodes revealed that the capacity decay during the first 20 cycles, especially for LVO electrodes, could be attributed to the shuttling of the interlayer structural water rather than layered structure disordering or irreversible structural transformation.

The rate capabilities of LVO, MVO, LMVO, and LMVO-200 electrodes are shown in **Figure 7c**. The LVO electrode exhibited capacity degradation as the current density increase, as it only retained ~70 mAh $g^{-1}$ and ~30 mAh $g^{-1}$ at current densities of 100 and 200 mA $g^{-1}$, respectively. The MVO electrode, delivered ~120 mAh $g^{-1}$ at 100 mA $g^{-1}$ and ~95 mAh $g^{-1}$ at 200 mA $g^{-1}$, performing better compared to LVO electrode. The LMVO and LMVO-200 electrodes exhibited a similar cycling characteristic as the cycle life test in the first 10 cycles. As the current density increase, the LMVO electrode delivered ~220 mAh $g^{-1}$ at 50 mAh $g^{-1}$, ~190 mAh $g^{-1}$ at 100 mA $g^{-1}$, and ~165 mAh $g^{-1}$ at 200 mA $g^{-1}$, suggesting the rate capability was significantly improved by simultaneous preintercalation of $Li^+$ and $Mg^{2+}$ ions. The specific capacity of LMVO electrode decreased by ~17 mAh $g^{-1}$, ~15 mAh $g^{-1}$, and ~18 mAh $g^{-1}$ as the current densities increased from 20 to 50 mA $g^{-1}$, 50 to 100 mA $g^{-1}$, and 100 to 200 mA $g^{-1}$, respectively. In comparison, the specific capacity of LMVO-200 electrode decreased by only ~18 mAh $g^{-1}$, ~10 mAh $g^{-1}$, and 12 mAh $g^{-1}$ under the same conditions, suggesting a further enhanced rate capabilities due to partial dehydration enabled

View Article Online
DOI: 10.1039/D5TA00673B

via vacuum-drying. When current density was set back to 20 mA g$^{-1}$, LVO electrode only remains ~150 mAh g$^{-1}$, which is significantly lower than the first 10 cycles at 20 mA g$^{-1}$. The recovered specific capacities of the MVO, LMVO, and LMVO-200 electrodes at 20 mA g$^{-1}$ were ~140, ~210, and ~190 mAh g$^{-1}$, respectively, each declining by ~30 mAh g$^{-1}$ compared to their specific capacities during the first 10 cycles.

The diffusion coefficients shown in **Figure 7d**, derived from GITT experiments (**Supporting Information, Figure S5**), indicate that the dual metal-ion preintercalation enables higher diffusion coefficients of $Li^+$ ions in LMVO electrodes compared to the single metal-ion pre-intercalated LVO or MVO electrodes. After vacuum drying treatment, the LMVO-200 electrodes demonstrated the highest diffusion coefficients in this study, which could be attributed to the partial dehydration that further enhances the synergistic effect of $Li^+$ and $Mg^{2+}$ dual metal-ion preintercalation. In general, LMVO-200 demonstrated the best overall electrochemical performance in Li-ion cells, that is attributed to the simultaneous preintercalation of electrochemically active $Li^+$ and structure stabilizing $Mg^{2+}$ ions, followed by vacuum-drying procedure that minimizes the content of structure water without phase transformation, which led the charge contribution from surface-controlled capacitive partially shifted to diffusion-limited processes, and suppressed the irreversible parasitic reaction between $Li^+$ ions and structural water.

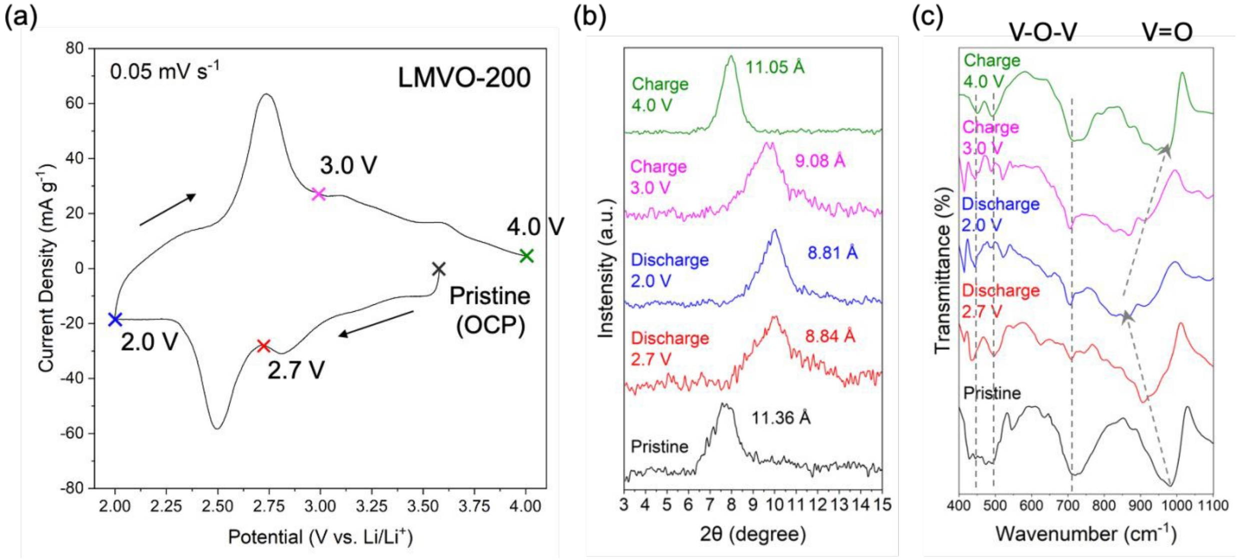

**Figure 8.** (a) CV curve of the LMVO-200 electrode scanned at 0.05 mV s$^{-1}$ with the indication of the open circuit potential (OCP) and potentials at which ex-situ XRD and FTIR analyses were performed: 2.7 V (discharge), 2.0 V (discharge) , 3.0 V (charge), and 4.0 V (charge); (b) ex-situ XRD patterns and (c) ex-situ ATR FTIR analysis of the vanadium oxide fingerprint region, for the LMVO-200 electrodes at the selected potentials, respectively.

To investigate the local and bulk structure evolution of the dual metal ion preintercalated and partially dehydrated BVO electrodes during electrochemical cycling, post-cycled LMVO-200 electrodes at different

View Article Online
DOI: 10.1039/D5TA00673B

potentials were analyzed using ex-situ XRD and FTIR techniques. The CV curve of the studied electrode is shown in **Figure 8(a)**, indicating the cut-off potentials selected for the ex-situ XRD and FTIR analysis. The (001) reflection in the XRD patterns of the pristine LMVO-200 electrode, shown in **Figure 8(b)**, indicate that the interlayer distance of LMVO-200 slightly increased from 10.98 Å (from its powder XRD) to 11.36 Å during the electrode preparation steps, but generally retained its layered structure. As the discharge progressed from OCP (~3.55 V) to 2.0 V, the (001) reflection shifted to a higher 2θ angle, indicating a decrease in the interlayer distance of LMVO-200 to 8.81 Å due to the electrochemical intercalation of $Li^+$ ions. The increase in potential up to 4.0 V on charge cycle, corresponding to the extraction of $Li^+$ ions, led to a low-angle shift of the (001) reflection that correspond to the increase of interlayer distance to 11.05 Å, revealing the "lattice breathing effect" and good stability of the layered crystal structure of LMVO-200 upon a reversible electrochemical cycle. The FTIR spectra of the LMVO-200 electrodes in the BVO fingerprint region, revealing the structural changes within the V-O bilayers at various potentials, are shown in **Figure 8(c)**. The FTIR spectrum of the pristine LMVO-200 electrode exhibits similar characteristics to its powder FTIR spectrum, primarily featuring three bands corresponding to V-O-V out-of-plane, V-O-V in-plane, and V=O stretching at wavenumbers of ~500 $cm^{-1}$, ~720 $cm^{-1}$, and ~1000 $cm^{-1}$, respectively. The band at ~1000 $cm^{-1}$, indicating the stretching of V=O, shifts to a lower wavenumber and broadens significantly upon discharge, suggesting a shortening of the atomic distance between vanadium and cap oxygen. Additionally, the intensities of the V-O-V out-of-plane and in-plane bands at ~500 and ~720 $cm^{-1}$ attenuate significantly upon discharge, indicating a loss of bilayered ordering within the V-O 2D slabs. However, when the electrode's potential is restored to 4.0 V, the V-O slabs revert to their bilayered structure, as the characteristics of bilayered vanadium oxide reappear in the ex-situ FTIR spectrum at 4.0 V. The combination of XRD and FTIR ex-situ analyses revealed that the excellent cycling stability of LMVO-200 electrode is attributed to its good structural reversibility, from the aspect of bulk (inter-bilayer) and local (intra-bilayer) structures, during electrochemical operation in Li-ion cells.

This work not only experimentally demonstrated the non-aqueous cycling performance of layered electrode materials can be advanced via engineering the chemistries of the interlayer regions, but also elucidated the role of multi-species ($Li^+$, $Mg^{2+}$, and structural $H_2O$) from the interlayer regions of electrode material in rechargeable Li-ion batteries. The tuning of chemistries from the interlayer regions highlighted the opportunities of advancing charge storage properties of other layered electrode materials with large interlayer spacing (e.g., layered manganese [49] and tungsten oxide [54, 55]) for beyond non-aqueous electrolyte and beyond lithium-ion chemistries, as the electrochemically inactive ion could be identified (the electrochemical active ion is obvious). Additionally, developing new layered electrode materials using this methodology requires the innovation of new synthesis methods and processing approaches to achieve a desired structure and chemistry. The ex-situ XRD and ATR FTIR analysis in this work emphasized that

View Article Online
DOI: 10.1039/D5TA00673B

understanding the intra-layer structure evolution and reversibility is equally important as the widely investigated and acknowledged inter-layer structural evolution during electrochemical operation. A similar experiment protocol or methodology could be established to holistically study the structural evolution of layered electrode materials for a better understanding of the charge storage and degradation mechanisms, therefore fostering the availability of better materials for electrochemical energy storage technologies.

# Conclusions

In this work, we demonstrated a feasible two-step synthesis route, including the chemical preintercalation of magnesium followed by hydrothermal treatment in a LiCl solution, that allowed to simultaneously introduce 0.19 $Li^+$ and 0.10 $Mg^{2+}$ ions into the interlayer region of nanostructured BVO, producing a material with the chemical formula of $\delta\text{-}Li_{0.19}Mg_{0.10}V_2O_5\cdot 0.85H_2O$. Through low-temperature vacuum-drying, the hydration degree ($n$ in $\delta\text{-}Li_{0.19}Mg_{0.10}V_2O_5\cdot nH_2O$) was reduced from 0.85 to 0.67 without phase transformation. By comparing the BVO polymorphs with individually preintercalated $Li^+$ or $Mg^{2+}$ ions, we experimentally demonstrated that the specific capacity and cycling stability of BVOs can be improved by the simultaneous preintercalation of $Li^+$ and $Mg^{2+}$ ions, which act as species that facilitate diffusion and stabilize the structure during electrochemical cycling in Li-ion cells, respectively. The *b*-value analyses revealed that the preintercalation of $Li^+$ enhances the surface-controlled charge storage process, while the preintercalation of $Mg^{2+}$ promotes the charge storage contribution from the diffusion-limited process. By comparing the *b*-values determined for LMVO and LMVO-200 electrodes, we experimentally demonstrated that the surface-controlled charge transport process can be further facilitated by interlayer structural water, enabling a higher capacity of the LMVO electrode. By preintercalating two types of metal ions simultaneously, $\delta\text{-}Li_{0.19}Mg_{0.10}V_2O_5\cdot 0.85H_2O$ exhibited synergistic improvements in specific capacity and cycling stability, delivering 245 mAh $g^{-1}$ during the initial discharge cycles and retaining ~58% of its capacity after 50 cycles. This cycling stability is comparable to the ~57% capacity retention of MVO ($\delta\text{-}Mg_{0.22}V_2O_5\cdot 0.92H_2O$) and significantly higher than the 22% retention observed for LVO, achieved without any notable significant sacrifice in specific capacity. The dual metal ion preintercalated and vacuum-dried $\delta\text{-}Li_{0.19}Mg_{0.10}V_2O_5\cdot 0.67H_2O$ electrode retained ~66% of its initial specific capacity after 100 cycles. This improvement is attributed to the reduction of structural water, which leads to a transition from a surface-controlled process to a diffusion-limited process while simultaneously suppressing water-related parasitic reactions. The diffusion coefficients, derived from GITT experiments, suggested that the simultaneous preintercalation of $Li^+$ and $Mg^{2+}$ ions combined with the vacuum-drying step at 200°C effectively facilitated the diffusion of $Li^+$ ions, compared to the single metal ion preintercalated electrodes. Through both diffusion coefficients and *b*-values analysis, we conclude that the preintercalated $Li^+$ ions define specific diffusion sites in the interlayer regions during synthesis, leading to the increased capacity due to higher $Li^+$

View Article Online
DOI: 10.1039/D5TA00673B

diffusion coefficient; and the preintercalated $Mg^{2+}$ ions substantially improve the cycling stability without significantly sacrificing the specific capacity by promoting the diffusion-limited charge storage contribution. Through post-cycled analysis of electrodes via XRD and ATR FTIR, the excellent cycling stability of the $\delta$-$Li_{0.19}Mg_{0.10}V_2O_5 \cdot 0.67H_2O$ electrode in Li-ion cells was attributed to its highly robust intra- and inter-bilayer structure reversibility during electrochemical operation. By experimentally demonstrating that specific capacity and cycling stability can be synergistically enhanced through dual metal ion preintercalation, this work underscores the importance of understanding the role of multiple interlayer species introduced during synthesis and processing steps. Furthermore, it suggests that similar studies could be extended to other layered electrodes and energy storage systems beyond Li-ion batteries.

## Acknowledgments

This work was supported by the National Science Foundation grant DMR-2106445. The XRD, SEM and XPS analyses were conducted using instruments in the Materials Characterization Core (MCC) at Drexel University. We thank Prof. Kevin Owens from the Department of Chemistry at Drexel University for providing us with access to the atomic absorption spectroscopy analysis in the Instrumental Analytical Laboratory.

View Article Online
DOI: 10.1039/D5TA00673B

# References

(1) Manthiram, A. A reflection on lithium-ion battery cathode chemistry. *Nature Communications* **2020**, *11* (1), 1550. DOI: 10.1038/s41467-020-15355-0.

(2) Chen, K.; Barai, P.; Kahvecioglu, O.; Wu, L.; Pupek, K. Z.; Ge, M.; Ma, L.; Ehrlich, S. N.; Zhong, H.; Zhu, Y.; et al. Cobalt-free composite-structured cathodes with lithium-stoichiometry control for sustainable lithium-ion batteries. *Nature Communications* **2024**, *15* (1), 430. DOI: 10.1038/s41467-023-44583-3.

(3) Lauro, S. N.; Burrow, J. N.; Mullins, C. B. Restructuring the lithium-ion battery: A perspective on electrode architectures. *eScience* **2023**, *3* (4), 100152. DOI: https://doi.org/10.1016/j.esci.2023.100152.

(4) Zhang, G.; Li, M.; Ye, Z.; Chen, T.; Cao, J.; Yang, H.; Ma, C.; Jia, Z.; Xie, J.; Cui, N.; et al. Lithium Iron Phosphate and Layered Transition Metal Oxide Cathode for Power Batteries: Attenuation Mechanisms and Modification Strategies. *Materials* **2023**, *16* (17), 5769.

(5) Huang, Y.; Dong, Y.; Li, S.; Lee, J.; Wang, C.; Zhu, Z.; Xue, W.; Li, Y.; Li, J. Lithium Manganese Spinel Cathodes for Lithium-Ion Batteries. *Advanced Energy Materials* **2021**, *11* (2), 2000997. DOI: https://doi.org/10.1002/aenm.202000997.

(6) Akhilash, M.; Salini, P. S.; John, B.; Mercy, T. D. A journey through layered cathode materials for lithium ion cells – From lithium cobalt oxide to lithium-rich transition metal oxides. *Journal of Alloys and Compounds* **2021**, *869*, 159239. DOI: https://doi.org/10.1016/j.jallcom.2021.159239.

(7) Abraham, K. M. How Comparable Are Sodium-Ion Batteries to Lithium-Ion Counterparts? *ACS Energy Letters* **2020**, *5* (11), 3544-3547. DOI: 10.1021/acsenergylett.0c02181.

(8) Peng, L.; Zhu, Y.; Chen, D.; Ruoff, R. S.; Yu, G. Two-Dimensional Materials for Beyond-Lithium-Ion Batteries. *Advanced Energy Materials* **2016**, *6* (11), 1600025. DOI: https://doi.org/10.1002/aenm.201600025.

(9) Ming, L.; Ruzi, M.; Anting, D.; Kai, Z.; Fan, G.; Chengliang, X. Electrochemical technology to drive spent lithium-ion batteries (LIBs) recycling: recent progress, and prospects. *Energy Materials* **2024**, *4* (6), 400070. DOI: 10.20517/energymater.2024.29.

(10) Moretti, A.; Passerini, S. Bilayered Nanostructured $V_2O_5 \cdot nH_2O$ for Metal Batteries. *Advanced Energy Materials* **2016**, *6* (23), 1600868. DOI: https://doi.org/10.1002/aenm.201600868.

(11) Tepavcevic, S.; Xiong, H.; Stamenkovic, V. R.; Zuo, X.; Balasubramanian, M.; Prakapenka, V. B.; Johnson, C. S.; Rajh, T. Nanostructured Bilayered Vanadium Oxide Electrodes for Rechargeable Sodium-Ion Batteries. *ACS Nano* **2012**, *6* (1), 530-538. DOI: 10.1021/nn203869a.

(12) Charles, D. S.; Feygenson, M.; Page, K.; Neuefeind, J.; Xu, W.; Teng, X. Structural water engaged disordered vanadium oxide nanosheets for high capacity aqueous potassium-ion storage. *Nature Communications* **2017**, *8* (1), 15520. DOI: 10.1038/ncomms15520.

(13) Kundu, D.; Adams, B. D.; Duffort, V.; Vajargah, S. H.; Nazar, L. F. A high-capacity and long-life aqueous rechargeable zinc battery using a metal oxide intercalation cathode. *Nature Energy* **2016**, *1* (10), 16119. DOI: 10.1038/nenergy.2016.119.

(14) Qi, P.; Wang, H.; Li, L.; Shen, X.; Ou, L.; Chen, M.; Lu, Y.; Hao, K.; Tang, Y. Facile Synthesis of Oxygen-Vacancy-Rich Li–K Coinsertion Vanadate Nanoflakes for High-Performance Zn-Ion Batteries. *ACS Sustainable Chemistry & Engineering* **2023**, *11* (40), 14691-14700. DOI: 10.1021/acssuschemeng.3c02616.

(15) Xu, X.; Xiong, F.; Meng, J.; Wang, X.; Niu, C.; An, Q.; Mai, L. Vanadium-Based Nanomaterials: A Promising Family for Emerging Metal-Ion Batteries. *Advanced Functional Materials* **2020**, *30* (10), 1904398. DOI: https://doi.org/10.1002/adfm.201904398.

View Article Online
DOI: 10.1039/D5TA00673B

(16) Ming, F.; Liang, H.; Lei, Y.; Kandambeth, S.; Eddaoudi, M.; Alshareef, H. N. Layered $Mg_xV_2O_5 \cdot nH_2O$ as Cathode Material for High-Performance Aqueous Zinc Ion Batteries. *ACS Energy Letters* **2018**, *3* (10), 2602-2609. DOI: 10.1021/acsenergylett.8b01423.

(17) Clites, M.; Byles, B. W.; Pomerantseva, E. Effect of aging and hydrothermal treatment on electrochemical performance of chemically pre-intercalated Na–V–O nanowires for Na-ion batteries. *Journal of Materials Chemistry A* **2016**, *4* (20), 7754-7761, 10.1039/C6TA02917E. DOI: 10.1039/C6TA02917E.

(18) Clites, M.; Hart, J. L.; Taheri, M. L.; Pomerantseva, E. Chemically Preintercalated Bilayered $K_xV_2O_5 \cdot nH_2O$ Nanobelts as a High-Performing Cathode Material for K-Ion Batteries. *ACS Energy Letters* **2018**, *3* (3), 562-567. DOI: 10.1021/acsenergylett.7b01278.

(19) Clites, M.; Pomerantseva, E. Bilayered vanadium oxides by chemical pre-intercalation of alkali and alkali-earth ions as battery electrodes. *Energy Storage Materials* **2018**, *11*, 30-37. DOI: 10.1016/j.ensm.2017.09.005.

(20) Ridley, P.; Gallano, C.; Andris, R.; Shuck, C. E.; Gogotsi, Y.; Pomerantseva, E. MXene-Derived Bilayered Vanadium Oxides with Enhanced Stability in Li-Ion Batteries. *ACS Applied Energy Materials* **2020**, *3* (11), 10892-10901. DOI: 10.1021/acsaem.0c01906.

(21) Zhang, X.; Andris, R.; Averianov, T.; Zachman, M. J.; Pomerantseva, E. Hybrid bilayered vanadium oxide electrodes with large and tunable interlayer distances in lithium-ion batteries. *Journal of Colloid and Interface Science* **2024**, *674*, 612-623. DOI: https://doi.org/10.1016/j.jcis.2024.06.164.

(22) Zhang, Y.; Xu, L.; Jiang, H.; Liu, Y.; Meng, C. Polyaniline-expanded the interlayer spacing of hydrated vanadium pentoxide by the interface-intercalation for aqueous rechargeable Zn-ion batteries. *Journal of Colloid and Interface Science* **2021**, *603*, 641-650. DOI: https://doi.org/10.1016/j.jcis.2021.06.141.

(23) Tong, Y.; Zang, Y.; Su, S.; Zhang, Y.; Fang, J.; Yang, Y.; Li, X.; Wu, X.; Chen, F.; Hou, J.; et al. Methylene blue intercalated vanadium oxide with synergistic energy storage mechanism for highly efficient aqueous zinc ion batteries. *Journal of Energy Chemistry* **2023**, *77*, 269-279. DOI: https://doi.org/10.1016/j.jechem.2022.10.040.

(24) Christensen, C. K.; Sørensen, D. R.; Hvam, J.; Ravnsbæk, D. B. Structural Evolution of Disordered $Li_xV_2O_5$ Bronzes in $V_2O_5$ Cathodes for Li-Ion Batteries. *Chemistry of Materials* **2019**, *31* (2), 512-520. DOI: 10.1021/acs.chemmater.8b04558.

(25) Wangoh, L. W.; Huang, Y.; Jezorek, R. L.; Kehoe, A. B.; Watson, G. W.; Omenya, F.; Quackenbush, N. F.; Chernova, N. A.; Whittingham, M. S.; Piper, L. F. J. Correlating Lithium Hydroxyl Accumulation with Capacity Retention in $V_2O_5$ Aerogel Cathodes. *ACS Applied Materials & Interfaces* **2016**, *8* (18), 11532-11538. DOI: 10.1021/acsami.6b02759.

(26) Pomerantseva, E. Chemical Preintercalation Synthesis of Versatile Electrode Materials for Electrochemical Energy Storage. *Accounts of Chemical Research* **2022**. DOI: 10.1021/acs.accounts.2c00193.

(27) Clites, M.; Hart, J. L.; Taheri, M. L.; Pomerantseva, E. Annealing-Assisted Enhancement of Electrochemical Stability of Na-Preintercalated Bilayered Vanadium Oxide Electrodes in Na-Ion Batteries. *ACS Applied Energy Materials* **2020**, *3* (1), 1063-1075. DOI: 10.1021/acsaem.9b02098.

(28) Xu, Y.; Deng, X.; Li, Q.; Zhang, G.; Xiong, F.; Tan, S.; Wei, Q.; Lu, J.; Li, J.; An, Q.; et al. Vanadium Oxide Pillared by Interlayer Mg2+ Ions and Water as Ultralong-Life Cathodes for Magnesium-Ion Batteries. *Chem* **2019**, *5* (5), 1194-1209. DOI: https://doi.org/10.1016/j.chempr.2019.02.014.

View Article Online
DOI: 10.1039/D5TA00673B

(29) Jeon, B.; Kwak, H. H.; Hong, S.-T. Bilayered $Ca_{0.28}V_2O_5 \cdot H_2O$: High-Capacity Cathode Material for Rechargeable Ca-Ion Batteries and Its Charge Storage Mechanism. *Chemistry of Materials* **2022**, *34* (4), 1491-1498. DOI: 10.1021/acs.chemmater.1c02774.

(30) Zhao, Y.; Han, C.; Yang, J.; Su, J.; Xu, X.; Li, S.; Xu, L.; Fang, R.; Jiang, H.; Zou, X.; et al. Stable Alkali Metal Ion Intercalation Compounds as Optimized Metal Oxide Nanowire Cathodes for Lithium Batteries. *Nano Letters* **2015**, *15* (3), 2180-2185. DOI: 10.1021/acs.nanolett.5b00284.

(31) Fleischmann, S.; Zhang, Y.; Wang, X.; Cummings, P. T.; Wu, J.; Simon, P.; Gogotsi, Y.; Presser, V.; Augustyn, V. Continuous transition from double-layer to Faradaic charge storage in confined electrolytes. *Nature Energy* **2022**, *7* (3), 222-228. DOI: 10.1038/s41560-022-00993-z.

(32) Jiang, H.; Zhang, Y.; Waqar, M.; Yang, J.; Liu, Y.; Sun, J.; Feng, Z.; Sun, J.; Pan, Z.; Meng, C.; et al. Anomalous $Zn^{2+}$ Storage Behavior in Dual-Ion-In-Sequence Reconstructed Vanadium Oxides. *Advanced Functional Materials* **2023**, *33* (7), 2213127. DOI: https://doi.org/10.1002/adfm.202213127.

(33) Feng, Z.; Zhang, Y.; Sun, J.; Liu, Y.; Jiang, H.; Cui, M.; Hu, T.; Meng, C. Dual ions enable vanadium oxide hydration with superior $Zn^{2+}$ storage for aqueous zinc-ion batteries. *Chemical Engineering Journal* **2022**, *433*, 133795. DOI: https://doi.org/10.1016/j.cej.2021.133795.

(34) Bai, S.; Wang, X.; Wang, Q.; Chen, Z.; Zhang, Y. Bimetallic Intercalated Vanadium Oxide As a High-Performance Cathode for Aqueous Zinc Ion Batteries. *ACS Applied Materials & Interfaces* **2024**, *16* (17), 22403-22410. DOI: 10.1021/acsami.4c01648.

(35) Li, Z.; Yang, L.; Wang, S.; Zhu, K.; Li, H. Co-insertion of $K^+$ and $Ca^{2+}$ in vanadium oxide as high-performance aqueous zinc-ion battery cathode material. *Journal of Alloys and Compounds* **2024**, *992*, 174589. DOI: https://doi.org/10.1016/j.jallcom.2024.174589.

(36) Liu, C.; Zhang, L.; Chen, D.; Jiang, K. Dual ions pre-intercalated hydrate vanadium oxide as cathode drives high-performance aqueous zinc ions storage. *Journal of Alloys and Compounds* **2023**, *947*, 169476. DOI: https://doi.org/10.1016/j.jallcom.2023.169476.

(37) Liu, W.; Liu, X.; Ning, F.; Subhan, S.; Liu, Y.; Li, Q.; Zhang, J.; Lu, S.; Yi, J. Fabrication of a heterovalent dual-cation pre-embedded hydrated vanadium oxide cathode for high-performance zinc ion storage. *Journal of Materials Chemistry A* **2024**, 10.1039/D4TA00376D. DOI: 10.1039/D4TA00376D.

(38) Wang, J.; Zhao, X.; Kang, J.; Wang, X.; Yu, H.; Du, C.-F.; Yan, Q. $Li^+$, $Na^+$ co-stabilized vanadium oxide nanobelts with a bilayer structure for boosted zinc-ion storage performance. *Journal of Materials Chemistry A* **2022**, *10* (40), 21531-21539, 10.1039/D2TA05803K. DOI: 10.1039/D2TA05803K.

(39) Li, S.; Jia, X.; Liu, J.; Liu, Z.; Cao, G. Engineering hydrated vanadium oxide by $K^+$ and $Ni^{2+}$ incorporation for aqueous zinc ion batteries. *Materials Chemistry and Physics* **2022**, *287*, 126358. DOI: https://doi.org/10.1016/j.matchemphys.2022.126358.

(40) Yang, H.; Li, Q.; Sun, L.; Zhai, S.; Chen, X.; Tan, Y.; Wang, X.; Liu, C.; Deng, W.-Q.; Wu, H. MXene-Derived $Na^+$-Pillared Vanadate Cathodes for Dendrite-Free Potassium Metal Batteries. *Small* **2024**, *20* (5), 2306572. DOI: https://doi.org/10.1002/smll.202306572.

(41) Livage, J. Sol-gel chemistry and electrochemical properties of vanadium oxide gels. *Solid State Ionics* **1996**, *86-88*, 935-942. DOI: https://doi.org/10.1016/0167-2738(96)00336-0.

(42) Zhang, R.; Averianov, T.; Andris, R.; Zachman, M. J.; Pomerantseva, E. Liquid Phase Exfoliation of Chemically Prelithiated Bilayered Vanadium Oxide in Aqueous Media for Li-Ion Batteries. *The Journal of Physical Chemistry C* **2023**, *127* (2), 919-929. DOI: 10.1021/acs.jpcc.2c06875.

View Article Online
DOI: 10.1039/D5TA00673B

(43) Yang, Y.; Liu, G.; Fang, Z.; Liu, M.; Zhao, Y.; Lai, X.; Bi, J.; Gao, D. Dual-Guest Intercalated Vanadium Oxides with a Robust Channel for Efficient Zn Ion Diffusion and Storage. *ACS Sustainable Chemistry & Engineering* **2024**, *12* (10), 3941-3950. DOI: 10.1021/acssuschemeng.3c06125.

(44) Rui, X. H.; Ding, N.; Liu, J.; Li, C.; Chen, C. H. Analysis of the chemical diffusion coefficient of lithium ions in $Li_3V_2(PO_4)_3$ cathode material. *Electrochimica Acta* **2010**, *55* (7), 2384-2390. DOI: https://doi.org/10.1016/j.electacta.2009.11.096.

(45) Prześniak-Welenc, M.; Łapiński, M.; Lewandowski, T.; Kościelska, B.; Wicikowski, L.; Sadowski, W. The Influence of Thermal Conditions on $V_2O_5$ Nanostructures Prepared by Sol-Gel Method. *Journal of Nanomaterials* **2015**, *2015* (1), 418024. DOI: https://doi.org/10.1155/2015/418024.

(46) Sanchez, C.; Livage, J.; Lucazeau, G. Infrared and Raman study of amorphous $V_2O_5$. *Journal of Raman Spectroscopy* **1982**, *12* (1), 68-72. DOI: https://doi.org/10.1002/jrs.1250120110.

(47) Averianov, T. Z., Xinle; Andris, Ryan; Olds, Daniel; Zachman, Michael; Pomerantseva, Ekaterina. The Influence of MAX phase etching conditions on the synthesis and properties of $V_2CT_x$ MXene-derived K-preintercalated bilayered vanadium oxides in non-aqueous K-ion batteries. *ACS Applied Nano Materials* **2025**, *under review*.

(48) Yu, H.; Aakyiir, M.; Xu, S.; Whittle, J. D.; Losic, D.; Ma, J. Maximized crystal water content and charge-shielding effect in layered vanadate render superior aqueous zinc-ion battery. *Materials Today Energy* **2021**, *21*, 100757. DOI: https://doi.org/10.1016/j.mtener.2021.100757.

(49) Boyd, S.; Ganeshan, K.; Tsai, W.-Y.; Wu, T.; Saeed, S.; Jiang, D.-e.; Balke, N.; van Duin, A. C. T.; Augustyn, V. Effects of interlayer confinement and hydration on capacitive charge storage in birnessite. *Nature Materials* **2021**, *20* (12), 1689-1694. DOI: 10.1038/s41563-021-01066-4.

(50) Yan, M.; He, P.; Chen, Y.; Wang, S.; Wei, Q.; Zhao, K.; Xu, X.; An, Q.; Shuang, Y.; Shao, Y.; et al. Water-Lubricated Intercalation in $V_2O_5{\cdot}nH_2O$ for High-Capacity and High-Rate Aqueous Rechargeable Zinc Batteries. *Advanced Materials* **2018**, *30* (1), 1703725. DOI: https://doi.org/10.1002/adma.201703725.

(51) Zhao, Y.; Liang, S.; Shi, X.; Yang, Y.; Tang, Y.; Lu, B.; Zhou, J. Synergetic Effect of Alkali-Site Substitution and Oxygen Vacancy Boosting Vanadate Cathode for Super-Stable Potassium and Zinc Storage. *Advanced Functional Materials* **2022**, *32* (32), 2203819. DOI: https://doi.org/10.1002/adfm.202203819.

(52) Omo-Lamai, D.; Zhang, X.; Andris, R.; Zachman, M. J.; Pomerantseva, E. Chemical preintercalation of magnesium ions into α-$MoO_3$ structure for improved electrochemical stability in Li-ion cells. *Journal of Alloys and Compounds* **2024**, *1005*, 175954. DOI: https://doi.org/10.1016/j.jallcom.2024.175954.

(53) Yu, M.; Shao, H.; Wang, G.; Yang, F.; Liang, C.; Rozier, P.; Wang, C.-Z.; Lu, X.; Simon, P.; Feng, X. Interlayer gap widened α-phase molybdenum trioxide as high-rate anodes for dual-ion-intercalation energy storage devices. *Nature Communications* **2020**, *11* (1), 1348. DOI: 10.1038/s41467-020-15216-w.

(54) Mitchell, J. B.; Lo, W. C.; Genc, A.; LeBeau, J.; Augustyn, V. Transition from Battery to Pseudocapacitor Behavior via Structural Water in Tungsten Oxide. *Chemistry of Materials* **2017**, *29* (9), 3928-3937. DOI: 10.1021/acs.chemmater.6b05485.

(55) Mitchell, J. B.; Wang, R.; Ko, J. S.; Long, J. W.; Augustyn, V. Critical Role of Structural Water for Enhanced $Li^+$ Insertion Kinetics in Crystalline Tungsten Oxides. *Journal of The Electrochemical Society* **2022**, *169* (3), 030534. DOI: 10.1149/1945-7111/ac58c8.

View Article Online
DOI: 10.1039/D5TA00673B

# Data Availability Statements

Data for this article, including XRD, TGA, FTIR, AAS, XPS, and electrochemical analyses are available at *Materials Commons 2.0* at https://doi.org/10.13011/m3-s85w-cv37.